

TUMOR-INFILTRATING NOCICEPTOR NEURONS PROMOTE IMMUNOSUPPRESSION

Short title: Cancer, nerves and immune suppression.

Anthony C. Restaino¹, Maryam Ahmadi², Amin Reza Nikpoor², Austin Walz¹,
Mohammad Balood², Tuany Eichwald^{2,3}, Sebastien Talbot^{2,3}, Paola D. Vermeer^{1,*}

¹ Cancer Biology and Immunotherapies Group, Sanford Research, Sioux Falls, USA

² Department of Biomedical and Molecular Sciences, Queen's University, Kingston, Canada

³ Department of Physiology and Pharmacology, Karolinska Institutet, Solna, Sweden.

* corresponding author: Paola.Vermeer@sanfordhealth.org

Abstract

Nociceptor neurons impact tumor immunity. Removing nociceptor neurons reduced myeloid-derived suppressor cell (MDSCs) tumor infiltration in mouse models of head and neck carcinoma and melanoma. Carcinoma-released small extracellular vesicles (sEVs) attract nociceptive nerves to tumors. sEV-deficient tumors fail to develop in mice lacking nociceptor neurons. Exposure of dorsal root ganglia (DRG) neurons to cancer sEVs elevated expression of Substance P, IL-6 and injury-related neuronal markers while treatment with cancer sEVs and cytotoxic CD8 T-cells induced an immunosuppressive state (increased exhaustion ligands and cytokines). Cancer patient sEVs enhanced DRG responses to capsaicin, indicating increased nociceptor sensitivity. Conditioned media from DRG and cancer cell co-cultures promoted expression of MDSC markers in primary bone marrow cells while DRG conditioned media together with cancer sEVs induced checkpoint expression on T-cells. Our findings indicate that nociceptor neurons facilitate CD8+ T cell exhaustion and enhance MDSC infiltration. Targeting nociceptor-released IL-6 emerges as a novel strategy to disrupt harmful neuro-immune interactions in cancer and enhance anti-tumor immunity.

Introduction

Head and neck squamous cell carcinomas (HNSCCs) are a collection of epithelial tumors that arise in the oral and oropharyngeal cavities (1-3); these cancers account for the sixth most common cancer diagnosed (4). HNSCCs are separated into two groups based on the mechanism of disease initiation; those induced by infection with high-risk human papillomaviruses (HPV⁺) and those that are mutationally driven through exposure to carcinogens such as alcohol and/or tobacco use (HPV⁻) (5, 6). While standard chemotherapy-radiation therapy provides excellent results for primary HNSCC, recurrence and metastasis remain a major challenge (7, 8). Recent advancements in immunotherapy offer additional options, but effects remain inconsistent with many patients failing to show improvement (9). As a result, efforts focused on identifying factors within the tumor environment that impact response to treatment continue. One such factor, includes the presence and functions of tumor-infiltrating nerves.

HNSCCs originate in areas rich with neuronal structures, including several cranial nerves. We have determined that HNSCC innervation primarily involves TRPV1-expressing nociceptor

48 neurons from the trigeminal ganglia (TGM) (10). Similarly, melanoma is innervated by these
49 neurons which are known to interact with both the innate and adaptive immune systems (11, 12).
50 Neuro-immune crosstalk is crucial in regulating immune responses in infectious diseases (13, 14)
51 and autoimmune disorders (15, 16). Recent studies in cancer models have also identified neural-
52 immune interactions (17). In melanoma, sensory neurons facilitate the recruitment of myeloid-
53 derived suppressor cells (MDSCs) and induce CD8⁺ T cell exhaustion via the release of calcitonin
54 gene-related peptide (CGRP) (18, 19). However, the initiating mechanisms behind this neural-
55 immune crosstalk in cancer are not fully understood.

56 Small extracellular vesicles (sEVs) are membrane-bound vesicles, measuring
57 approximately 50-150nm in diameter, and are formed through the endocytic pathway (20).
58 Released by all cells, sEVs serve as critical mediators of cell-to-cell communication both locally
59 and at a distance (21). These vesicles carry a diverse array of biological materials, including
60 proteins, lipids, and nucleic acids (21), and play a pivotal role in disease progression by
61 contributing to metastasis and the remodeling of the tumor microenvironment (22-24). Integrins,
62 embedded in the membranes of sEVs, are particularly crucial for targeting and preparing
63 metastatic sites (25). The impact of sEVs on cancer progression, treatment resistance, and
64 metastasis has been documented in various cancer, including HNSCC (21, 26, 27). Additionally,
65 sEVs attract loco-regional neurons into the tumor milieu (26, 27), influencing local neuronal
66 function and pain sensitization in murine models of oral cancer, thus underscoring their
67 significant role in neuronal reprogramming and functionality (27).

68 We now employ syngeneic models of HNSCC and melanoma to explore the interaction
69 between tumor-infiltrating nociceptor neurons, tumor cells and infiltrative immune cells. Our
70 studies aim to determine the effects of nociceptor neuron loss on local tumor-associated immune
71 cell populations. Additionally, we investigate whether tumors modify neuronal functions and, if
72 so, assess how these changes contribute to the immunosuppressive environment within these
73 cancers.

74 **Results**

75 *sEV-mediated recruitment of nociceptor neurons is essential for disease initiation*

76 The HPV⁺ HNSCC syngeneic murine cell line, mEERL cells, drive tumor innervation via release
77 of sEVs (26, 27); this innervation promotes tumor growth as it is reduced when mEERL cells are
78 implanted in nociceptor neuron-ablated mice (10). We have reproduced these data and now seek
79 to examine whether compromising sEVs release in mEERL cells further impacts their growth in
80 nociceptor ablated mice. To explore this, we used a mEERL cell variant where CRISPR-Cas9
81 technology deleted Rab27a and b, GTPases necessary for sEV release (26). When implanted into
82 C57BL/6 mice, these cells exhibited reduced tumor growth (**Fig. 1**). Of note, tumor growth was
83 completely blocked when the sEV-compromised cells (mEERL Rab27^{-/-}) were implanted into
84 nociceptor neuron-ablated mice (**Fig. 1**). This result was reproduced across three experiments
85 involving 25 animals per group and suggests that sEV-mediated recruitment of nociceptor
86 neurons is essential for disease initiation.

87

88 *Tumor-infiltrating neurons are transcriptionally modified*

89 We hypothesized that tumor-released sEVs alter neuronal gene expression and function, thereby
90 impacting disease initiation. To test this, mEERL cells were orthotopically implanted into
91 C57BL/6 mice, and tumors were allowed to establish and grow. Twenty-five days post-tumor
92 implantation, we harvested the ipsilateral TGM ganglia from tumor-bearing mice, with the
93 contralateral TGM ganglia serving as controls. As expected from a previous study (28), the
94 analysis of neuronal RNA from these ganglia revealed significantly increased expression of *Atf3*,
95 a neuron-injury transcript, along with various regeneration-associated genes (RAGs) such as
96 *Gap43*, *Gadd45*, and *Sppr1a* (**Fig. 2A**). Further validation with an additional group of mEERL
97 tumor-bearing mice confirmed the increased expression of *Atf3* and markers of nociceptor

98 neurons (*Cgrp*, *Tac1*) and *Tubb3*, a neuronal marker, in ipsilateral TGM neurons (**Fig. 2B**).
99 Protein expression analysis by immunofluorescence confirmed our qPCR data (**Fig. 2C, D, Fig**
100 **S1**).

102 *Nociceptor neuron and mEERL cell interactions modulate the tumor milieu*

103 This neuron injury gene signature in tumor-infiltrating neurons led us to explore whether these
104 changes influenced the neuronal secretory profile. To investigate this, DRG neurons were co-
105 cultured with mEERL cells, and the resulting conditioned media analyzed using a cytokine array.
106 This co-culture resulted in an increased release of several factors, including IL-6, CCL2, CCL19,
107 CXCL5, CD30L, CxCl16, TIMP1 (**Fig. S2**) and SP (**Fig. 3A**). In a neuronal co-culture with
108 mEERL Rab27^{-/-} cells (compromised in sEV release), SP release was reduced (**Fig. 3A**). Further
109 experiments tested whether SP directly induced IL-6 release from mEERL cells. While baseline
110 IL-6 release was low in mEERL cells cultured alone, it significantly increased following
111 treatment with recombinant SP. Notably, we had previously shown that mEERL cells express the
112 SP receptor, NK1R (*10*); and now found that blocking this receptor in Substance P treated
113 mEERL cells negated the IL-6 release (**Fig. 3B**). Additionally, DRG neurons themselves released
114 more IL-6 when co-cultured with mEERL cells, an effect that was nullified by including an
115 NK1R antagonist (**Fig. 3C**). As opposed to wildtype DRG neurons, we cultured DRG neurons
116 from germline knockout IL-6 mice and found no detectable IL-6 in the conditioned media from
117 these neurons when co-cultured with mEERL cells (**Fig. 3D, Fig. S2**). IL-6 release was increased
118 when neurons were co-cultured with higher numbers of mEERL cells (**Fig. 3E**). Collectively,
119 these findings suggest that interactions between mEERL cells and nociceptor neurons, mediated
120 through both released sEVs and soluble factors like SP, led to increase IL-6 levels in the tumor
121 microenvironment.

123 *Ablation of nociceptor neurons decreases MDSCs in the mEERL tumor bed*

124 IL-6 has immunosuppressive action involving the expansion of MDSCs (29-31). Since we found
125 that neurons are a major source of IL-6, we next sought to measure the impact of tumor-
126 infiltrating nerves on tumor-infiltrating lymphocytes (TILs). We found that 25 days post tumor
127 implantation, a phase of active growth and innervation, mEERL tumors implanted in nociceptor
128 neuron ablated animals harbored a reduction in MDSCs and an increase in CD8⁺ T cells (**Fig.**
129 **4A**). Levels of CD4⁺ were not impacted (gating strategy shown in **Fig. S3**). To ensure that
130 differences in tumor volume did not influence the tumoral MDSC population, we harvested
131 tumors on day 15 post-implantation, when tumor volumes were comparable across the two
132 groups. MDSCs are known to be a heterogeneous group of immune cells with two primary
133 subtypes: monocytic MDSCs, which have high expression of Ly6C (Ly6C^{hi}Ly6G⁻), and
134 granulocytic MDSCs, marked by high expression of Ly6G (Ly6C^{lo}Ly6G⁺) (32, 33). Despite their
135 similar anti-tumor functions, these subtypes operate through distinctly different mechanisms (34).
136 Detailed TIL immunophenotyping revealed that tumors from nociceptor neuron ablated mice had
137 reduced numbers of granulocytic MDSC (**Fig. 4B**).

139 *Ablation of nociceptor neurons decreases MDSCs in melanoma and alters MDSC transcriptome*

140 As tumor-infiltrating nociceptor neurons appear to drive this phenotype, we sought to test whether
141 a similar phenotype could be observed in another densely innervated cancer. To test this, we used
142 the syngeneic melanoma model B16F10-OVA cells implanted intradermally into either
143 nociceptor ablated (*Trpv1^{cre}::DTA^{fl/wt}*) mice or their littermate controls (*Trpv1^{wt}::DTA^{fl/wt}*), the
144 latter showing reduced tumor growth (**Fig. 5A**). Similar to the results seen in mEERL tumors,
145 melanoma tumors from nociceptor neuron-ablated mice also showed a decreased MDSC
146 population fourteen days post-tumor implantation (**Fig 5B**). Although the specific subgroups of
147 MDSCs affected by the ablation of nociceptor neurons varied between mEERL and B16F10-

148 OVA tumors, the consistent influence of these neurons on MDSC recruitment across different
149 malignancies was evident. We next assessed the influence of nociceptor neurons on the MDSC
150 transcriptome. To do so, we FACS-purified MDSC from nociceptor intact and ablated mice and
151 profiled their transcriptome using RNA sequencing. We found ~500 differentially expressed
152 genes in nociceptor ablated mice, including decreases in *Csf1*, *Ill17rb*, *Motchl*, *Tgfb1*, *Il10* and
153 *Cxcl13* (**Fig. 5C, D**) all of which are known mediators of MDSC function (35, 36).

154 *Tumor cell-nociceptor neuron interactions induce MDSC differentiation from bone marrow cells*

155 Given that nociceptor neurons modified the transcriptome of MDSC, and that IL-6 is known to
156 drive their recruitment and expansion (29), we hypothesized that these tumor-infiltrating neurons
157 might drive the differentiation of bone marrow cells into MDSCs. We tested this by co-culturing
158 DRG neurons from nociceptor intact and ablated mice with sEV-competent or comprised mEERL
159 cells and used the conditioned media to treat bone marrow cells harvested from C57BL/6 mice
160 (**Fig. 6A**). Bone marrow cells stimulated with IL-6 and GM-CSF, which induces their
161 differentiation into MDSCs (37), served as a positive control. Untreated bone marrow cells served
162 as the negative control. As expected, IL-6 and GM-CSF stimulation significantly increased
163 expression of CD11b⁺/Gr1⁺, MDSC markers, on the bone marrow cells. The induction of these
164 markers was also robust in bone marrow cells stimulated with media from mEERL and wildtype
165 DRG co-cultures but reduced with mEERL-Rab27^{-/-} cells and DRG co-cultures (**Fig. 6B**). These
166 findings suggest that mEERL-released sEVs and DRG-released factors are crucial for MDSC
167 differentiation. No significant effects on expression of these MDSC markers were noted with
168 conditioned media that included nociceptor-ablated DRG, indicating a key role of nociceptor
169 neurons (**Fig. 6B, gating strategy in Fig. S3**). Quantitative PCR analysis of treated cells showed
170 that conditioned media from co-cultures of wildtype DRG and mEERL cells significantly induced
171 *Arg1*, *Cox2*, and *Cybb* expression, essential for MDSC immune suppression (38-40) (**Fig. 6C**).
172 These results highlight that mEERL cell/DRG interactions not only promote MDSC marker
173 expression (CD11b, Gr1) but also genes vital for their immune functions. Other conditioned
174 media had less impact, emphasizing the critical role of tumor cell/nociceptor neuron interactions
175 in shaping the tumor microenvironment and immune cell phenotypes.

176 *Tumor cell-nociceptor neuron interactions induce MDSC migration*

177 We next explored how mEERL/DRG interactions influence bone marrow cell migration to
178 tumors. DRG from nociceptor intact and ablated mice were cultured with mEERL cells or their
179 sEV-compromised variant (26). Concurrently, bone marrow cells from nociceptor intact mice
180 were treated with GM-CSF and IL-6 to differentiate them into MDSCs expressing CD11b and
181 Gr1 (37). After three days, these MDSCs were exposed to conditioned media from the
182 mEERL/DRG co-cultures in a transwell assay. 24 h later, migration analysis showed that
183 conditioned media from mEERL cells and wildtype DRG co-cultures led to the highest migration
184 levels. In contrast, media from DRG co-cultured with Rab27^{-/-} cells, which have impaired sEV
185 release, significantly reduced migration. These data highlight the strong migratory influence of
186 mEERL-released sEVs. The migration levels from nociceptor neuron-ablated DRG with mEERL
187 cells were similar to those from wildtype DRG with Rab27^{-/-} cells, indicating that nociceptor
188 neuron-derived factors significantly boost MDSC migration. The lowest migration occurred with
189 media from nociceptor-ablated DRG and mEERL-Rab27^{-/-} cells co-cultures (**Fig. 6D**).

192 *Nociceptor neurons and mEERL sEVs promote CD8⁺ T cell exhaustion*

193 To this point, our data reveals that nociceptor neurons influence the tumor microenvironment by
194 affecting both differentiation and recruitment of MDSCs to tumors, prompting further
195 examination of their impact on other immune cells. Moreover, our data suggest that CD8⁺ T cells
196 are increased in mEERL tumors from nociceptor-ablated animals (**Fig. 4A**). Notably, nociceptor
197

198 interactions with CD8⁺ T cells during bacterial infections inhibit immunity by releasing
199 neuropeptides (13, 14). Moreover, tumor released sEVs can directly impact CD8⁺ T cells (41).
200 Thus, we investigated whether nociceptor neurons and/or tumor sEVs also modulate CD8⁺ T
201 cells. Thus, we generated CD8⁺ T cells by activating splenocytes from C57BL/6 mice under T_{c1}
202 inflammatory conditions. These CD8⁺ T cells were then exposed to conditioned media from
203 wildtype DRG, mEERL sEVs, or both for four days. Analysis via flow cytometry showed that
204 DRG media increased PD-1, LAG3, and TIM3 co-expression, and decreased IFN γ and IL-2
205 production. mEERL sEVs alone had no effect, but their combination with DRG conditioned
206 media enhanced expression of these immune checkpoints and further reduced cytokine levels,
207 indicating that nociceptor neuron-released factors and tumor sEVs jointly promote CD8⁺ T cell
208 exhaustion (**Fig. 7A-C, gating strategy in Fig. S4**).

209 *mEERL sEVs and CD8⁺ T cells modulate the nociceptor neuron transcriptome*

210 Our *in vivo* data (**Fig. 2**) demonstrate that tumor-infiltrating neurons are transcriptionally
211 modified by the tumor microenvironment (TME). We hypothesized that mEERL sEVs or CD8⁺ T
212 cells (or both) contribute this effect. To test this, DRG neurons from TRPV1^{cre::tdTomato}^{fl/wt}
213 reporter mice were cultured alone or with mEERL-derived sEVs and/or CD8⁺ T cells. After 48h,
214 nociceptor neurons were FACS-purified, and RNA sequenced. Gene expression heatmaps
215 indicate the influence of mEERL sEVs and CD8⁺ T cells on the transcriptome of nociceptor
216 neurons. Among other changes, nociceptor neurons co-cultured with cytotoxic CD8⁺ T cells
217 increased their expression of pro-exhaustion ligands (Pd1, also known as CD274) and cytokines
218 (Il6), injury markers (Atf3, Sprr1a, Cryba2, Fgf3), and immunomodulatory neuropeptides (Gal,
219 Calca; **Fig. 8A-B**). Interestingly, the exposure to mEERL sEVs had the opposite effect,
220 decreasing some of the neuron reprogramming, including the injury markers (Atf3, Sprr1a,
221 Cryba2, Fgf3; **Fig. 8C-D**). Finally, when combining both mEERL-derived sEVs and CD8⁺ T cells
222 we drastically exacerbate nociceptor neurons reprogramming toward a pro-immunosuppressive
223 phenotype; as shown by increased expression of pro-exhaustion ligands (Pd1) and cytokines (Il6),
224 injury markers (Atf3, Sprr1a, Cryba2, Fgf3, Gpr151, Slc6a4, Ecel1), and immunomodulatory
225 neuropeptides (Gal; **Fig. 8E-F**). Along with this transcriptomic reprogramming, we sought to test
226 whether HNSCC patient-derived sEVs impact the response of nociceptor neurons to noxious
227 ligands. As a proxy for this response, we examined the influx of calcium in responses to the
228 TRPV1 agonist capsaicin (300 nM). Compared to neurons exposed to control sEVs, those
229 exposed to sEVs from HNSCC patients showed an increased response frequency to capsaicin
230 (**Fig. 8G**). These data are consistent with our *in vivo* findings (**Fig. 2**) and underscore the
231 contributions of mEERL sEVs and CD8⁺ T cells to the transcriptome and function of tumor-
232 infiltrating nociceptor neurons.

233 **Discussion**

234
235
236 The infiltration of cancers by nociceptor neurons highlights the complex interactions that
237 malignancies establish with their host, akin to the long-recognized connections of vascular and
238 immune systems with tumors (42-46). In this study, we focused on the neural influences on
239 disease progression, specifically in head and neck cancer and melanoma. Our findings
240 demonstrate that tumor-released sEVs together with CD8⁺ T cells alter the transcriptome and
241 sensitivity of tumor-infiltrating nociceptor neurons. Likely because of these changes, tumor-
242 infiltrating nociceptor neurons alter the factors they release, contributing to a pro-tumorigenic
243 tumor microenvironment.

244 Underlying these changes, we posit the existence of a feed-forward loop where tumor-
245 released sEVs stimulate SP release from nociceptor neurons. This neuropeptide then triggers IL-6
246 release from mEERL cells. Concurrently, soluble factors released from mEERL cells enhance IL-

247 6 production and release by nociceptor neurons. While our focus was primarily on IL-6, it is
248 important to note that other factors (CCL2, CCL19, CXCL5, CD30L, CxCl16, TIMP1) were also
249 induced by mEERL/nociceptor neuron co-cultures that likely also contribute to the tumor
250 microenvironment's immunosuppressive characteristics. These data matched the recent findings
251 from Von Andrian and colleagues showing neuronal release of CXCL5 and CCL2 (47) as well as
252 the one of Flavel presenting the release of IL-6 (48) For instance, one could imagine that the
253 neuronal release of CCL2 might be important for retaining conventional dendritic cells within the
254 tumors and the subsequent establishment of anti-tumor immunity.

255 Flow cytometric analysis reveals that this cytokine milieu recruits MDSCs to the tumor
256 bed, a process significantly diminished in tumors implanted in nociceptor neuron-ablated animals.
257 We demonstrated *in vitro* that this milieu not only stimulated MDSC differentiation and migration
258 but also that factors released by nociceptors together with mEERL sEVs modulated the
259 functionality of CD8⁺ T lymphocytes, enhancing their expression of immune checkpoint proteins
260 PD-1, LAG3, and TIM3, while reducing the production of IFN- γ and IL-2. Moreover, interactions
261 between mEERL sEVs and CD8⁺ T cells induce transcriptional changes on nociceptor neurons,
262 leading them to express a neuronal injury-associated transcriptome. These findings collectively
263 suggest that tumor cells, the neurons that infiltrate them, and the immune cells recruited to the site
264 collaboratively create an immunosuppressive environment, thereby contributing to disease
265 progression. This intricate interplay emphasizes the potential of targeting these neural and
266 molecular interactions in therapeutic strategies to combat cancer.

267 These findings underscore the necessity of reassessing the impact of immunotherapies on
268 patients with head and neck squamous cell carcinoma and melanoma, with consideration given to
269 incorporating nerve-targeting therapies. Current strategies for developing new therapeutic targets
270 in HNSCC are often inadequate which is partially due to the disease's heterogeneity (49, 50).
271 Although targeted therapies and immunotherapies represent significant advancements, their
272 outcomes have been generally disappointing (51-56)). For example, Cetuximab, a leading
273 targeted therapy for HNSCC, provides only modest clinical benefits with low response rates (57,
274 58). Similarly, PD-1 monoclonal antibody treatments like Pembrolizumab, though promising,
275 show variable success largely dependent on the specific immune phenotype of the patient's tumor
276 (59, 60).

277 Given these challenges, it is crucial to explore how a tumor's unique characteristics
278 modulates the microenvironment as this will influence treatment responses. Our study has
279 particularly focused on two pivotal immune cells, MDSCs and CD8⁺ T cells, which are integral to
280 cancer progression and demonstrate the influence of nociceptor neurons and tumor sEVs on their
281 number and functional status. Recent studies also highlight the significant role of the nervous
282 system, including sensory neurons, in altering the tumor immune environment (18, 19, 61-63).
283 Typically, neuro-immune interactions aim to maintain homeostasis, but tumor cells disrupt this
284 balance, promoting immunosuppression (64, 65). Our findings are consistent with this. This
285 maladaptive interaction suggests that targeting neurological pathways could complement existing
286 immunotherapies. For instance, experiments in melanoma mouse models showed that silencing
287 sensory neurons could enhance responses to anti-PD-L1 therapy, pointing to potential new
288 directions in oncologic treatment strategies (18).

289 The future of cancer therapy may increasingly incorporate neuron-targeting strategies.
290 This holistic view of the tumor microenvironment, which includes neural components, offers a
291 broader perspective for developing more effective and personalized cancer treatment strategies.
292 This could lead to innovative approaches that address not only the cancer cells but also the
293 complex interplay of biological systems that support tumor growth and survival.

294 **Materials and Methods**

296

297 Cell lines

298 The mEERL (RRID:CVCL_B6J3), and Rab27^{-/-} (mEERL-Rab27a^{-/-}/b^{-/+}), cell lines have been
299 characterized in previous studies (26, 66, 67). The mEERL and Rab27^{-/-} cells are cultured in E-
300 medium, which consists of DMEM (Corning, cat# 10-017-CV) mixed with Ham's F12 (Corning,
301 cat#10-080-CV), supplemented with 10% fetal calf serum, 1% penicillin/streptomycin, 0.5 µg/ml
302 hydrocortisone, 5 µg/ml transferrin, 5 µg/ml insulin, 1.36 ng/ml tri-iodothyronine, and 5 ng/ml
303 epidermal growth factor (EGF). All cell lines are cultured at 37°C in an environment containing
304 5% CO₂, and the culture medium is refreshed every three days.

305

306 Study approvals

307 Animal studies were conducted within the controlled environments of the Sanford Research
308 Animal Resource Center and a specific pathogen-free facility at Queen's University. All
309 procedures involving animals were conducted in accordance with the guidelines of the Canadian
310 Council on Animal Care (CCAC) and the Queen's University Animal Care Committee (UACC;
311 2023-2384).

312 Sanford Research has an Animal Welfare Assurance on file with the Office of Laboratory Animal
313 Welfare (assurance number is A-4568-01). Sanford Health is a licensed research facility under the
314 authority of the United States Department of Agriculture (USDA, certificate number 46-R-011).
315 The Sanford Health Animal Research Program is accredited by AAALAC, Intl. All animal
316 experiments conducted at Sanford Research were conducted under a Sanford Research approved
317 IACUC protocol and all experimenters complied with ARRIVE guidelines.

318

319 Animals.

320 Mice were housed in individually ventilated cages with access to water and subjected to 12-hour
321 light cycles; food was available ad libitum. C57BL/6/J (Jax #000664), TRPV1^{cre} (Jax #017769)
322 DTA^{fl/fl} (DTA; Jax #009669), were obtained from the Jackson Laboratory. As previously shown,
323 (18, 68-78) animals were bred in-house to generate littermate control (TRPV1^{wt}::DTA^{fl/wt}),
324 nociceptor reporter (Trpv1^{cre}::td-tomato^{fl/wt}) or ablated (*Trpv1*^{cre}::*DTA*^{fl/wt}) mice.

325

326 The Animal Resource Center (ARC) at Sanford Research is a specific pathogen-free facility.
327 Mice are maintained in IVC Tecniplast Green line Seal Safe Plus cages. These cages are only
328 opened under aseptic conditions in an animal transfer station. Aseptic technique is always used to
329 change animal cages every other week; all cages have individual HEPA filtered air. Animal
330 rooms are maintained at 75°F, 30-70% humidity, with a minimum of 15 air changes per h/cage.
331 Rooms are maintained with a 14:10 light/dark cycle. Corncob bedding and nesting materials are
332 autoclaved prior to use and are maintained in all cages. Animals were fed irradiated, sterile food
333 (Envigo) and given acidified water (pH 2.8-3.0) *ad libitum*. There are a maximum of 5 mice/cage.
334 Mice are observed daily by technicians. Abnormal behavior, signs of illness or distress, the
335 availability of food and water and proper husbandry are monitored.

336

337 Tumor implantation (mEERL and B16F10)

338 8-10-week-old C57BL/6 mice each weighed approximately 23 g at the start of experiments. The
339 animals were uniquely identified by ear punches and cage numbers, and the investigators were
340 blinded to group assignments when assessing the animals, such as during tumor measurements.

341

342 Orthotopic (oral cavity) mEERL tumor implantation:

343 Tumors were initiated into C57BL/6 mice as follows. Following anesthesia with ketamine (87.5
344 mg/kg)/xylazine (10mg/kg), each mouse was laid on its side. The mouth was gently opened, and

345 the lower lip grasped with a pair of tweezers and pulled down to extend the tissue. A 23–25-gauge
346 needle containing a suspension of mEERL cells was inserted into the crease of the mouse cheek,
347 along the mandible. 1×10^5 cells were slowly injected to orthotopically implant the cells in the
348 submucosal space. Mice were placed under a heat lamp to recover. Once fully recovered, they
349 were returned to their home cage. Mice were euthanized when tumor volume criteria were met,
350 approximately 500 mm^3 . Tumors were measured every 7 days using calipers. Prior to tumor
351 measurement, mice were anesthetized with isoflurane. Tumor volume was calculated using the
352 following equation: $(L \times W^2)/2$. Following euthanasia, tumors were extracted and utilized for
353 downstream assays.

354 Cell lines.

355 B16F10-mCherry-OVA (Matthew F. Krummel, UCSF), were cultured in complete Dulbecco's
356 Modified Eagle's Medium high glucose (DMEM, Corning, #10-013-CV) supplemented with 10%
357 fetal bovine serum (Seradigm, #3100) and 1% penicillin/streptomycin (Corning, #MT-3001-C1),
358 and maintained at 37°C in a humidified incubator with 5% CO_2 .

359 mEERL and mEERL Rab27^{-/-} cells were cultured as previously described (PMID: 30327461).
360 Briefly, cells were cultured in DMEM (Corning, cat# 10-017-CV)/Ham's F12 (Corning, cat# 10-
361 080-CV), 10% sEV-depleted fetal calf serum, 1% penicillin/streptomycin, 0.5 $\mu\text{g}/\text{ml}$
362 hydrocortisone, 5 $\mu\text{g}/\text{ml}$ transferrin, 5 $\mu\text{g}/\text{ml}$ insulin, 1.36 ng/ml tri-iodo-thyronine, and 5 ng/ml
363 EGF. The cells were maintained at 37°C in a humidified incubator with 5% CO_2 .

364 All the cell lines tested negative for mycoplasma, and none are listed by the International Cell
365 Line Authentication Committee registry (version 11). Non-commercial cell lines (B16F10-OVA)
366 were authenticated using antibody (against OVA, eGFP, mCherry) and/or imaging as well as
367 morphology and growth property. Commercial cell lines have not been further authenticated.

368 Melanoma inoculation and volume measurement

369 Cancer cells were resuspended in Phosphate Buffered Saline (PBS, Corning #21040CV) and
370 injected to the mice's skin right flank (5×10^5 cells; i.d., 100 μL). Growth was assessed daily using
371 a handheld digital caliper and tumor volume was determined by the formula $(L \times W^2 \times 0.52)$. L =
372 length and W = width.

373 Trigeminal (TGM) Ganglia isolation:

374 A midline incision was made on euthanized animals while in the prone position and this exposed
375 the crown of the skull. A transverse cut was used to separate the brainstem from the spinal cord
376 and the top of the skull was removed, thereby exposing the brainstem and TGM. The TGM
377 ganglia were then harvested and utilized for downstream assays.

378 Dorsal root ganglia isolation and co-culture

379 Dorsal root ganglia (DRG) were isolated from C57BL/6 or TRPV1^{cre}::DTA^{fl/wt} mice following
380 euthanasia. The mice were perfused with ice-cold HBSS and then underwent laminectomy to
381 expose the spinal cord, after which the DRG were excised and immediately placed in ice-cold
382 HBSS. The collected DRG were then embedded in 100 μl of CultureX (R&D Biosystems Cat#
383 3433-005-01) within a 30 mm cell culture dish. The CultureX was pipetted into the center of the
384 dish and allowed to sit at room temperature for 5 min before the DRG were inserted into the
385 matrix. Subsequently, the DRG were incubated at 37°C for 30 min, after which Ham's F-12
386 medium supplemented with 10% FBS was added to the dish. After an overnight incubation, the
387 DRG were either cultured alone or co-cultured with 3×10^4 mEERL or Rab27^{-/-} cells. Three days
388 later, conditioned media from these cultures were collected for downstream *ex vivo* experiments.

389 Ex vivo generation of myeloid derived suppressor cells

394 Male C57BL/6 mice were euthanized, and bone marrow cells were isolated from their long bones
395 following a previously described method (79). Briefly, the surrounding muscle tissue was grossly
396 removed from the long bones, which were then soaked in serum-free RPMI for 5 min to ease the
397 removal of any residual tissue. Subsequently, the bones were soaked in ethanol for another 5 min
398 to ensure sterilization before being thoroughly rinsed in HBSS to remove any traces of ethanol.
399 The epiphyseal ends of the bones were then cut open, and the marrow cells were flushed out by
400 injecting RPMI into the marrow cavity using a syringe fitted with a 25-gauge needle. Once
401 isolated, the bone marrow cells were cultured in RPMI supplemented with 10% fetal bovine
402 serum (FBS). To generate myeloid-derived suppressor cells (MDSCs), the bone marrow cells
403 were cultured in RPMI also containing 10% FBS, along with 40 ng/ml each of interleukin-6 (IL-
404 6) and granulocyte-macrophage colony-stimulating factor (GM-CSF).

405

406 Transwell migration assays

407 Bone marrow cells were harvested and stimulated to differentiate into MDSCs as described
408 above. 2×10^4 MDSCs were seeded onto a transwell (8 μm pore size, 3.0 μm polycarbonate
409 membrane, Costar, catalogue #34028). In the well below, 1 mL of conditioned media from the
410 designated co-cultures were added. Plates were kept in the incubator at 37°C for 12 h. The
411 number of MDSCs that migrated onto the underside of the transwell were analyzed as follows.
412 The top of the transwell was wiped with a Q-tip to remove all cells. The membrane was then fixed
413 with ethanol and stained with crystal violet. The inserts were left to dry at room temperature for
414 15 min before the membrane was removed and mounted onto a glass slide and the underside
415 (containing the migrated cells) analyzed by microscopy. ImageJ was utilized to quantify the
416 number of cells. $n=3$ wells/group were analyzed and the experiment was repeated twice with
417 similar results.

418

419 Flow cytometry of bone marrow cells

420 Bone marrow cells (BMCs) were harvested as previously described and seeded onto 50 mm
421 dishes each containing at least 2×10^5 cells. These bone marrow cells were treated with condition
422 media collected from mEERL cells, mEERL-Rab27^{-/-} cells, C57BL/6 DRG, TRPV1^{cre}::DTA^{fl/wt}
423 DRG, or their respective co-cultures (cancer cells and DRG). Positive controls were generated by
424 treating bone marrow cells with IL-6 and GM-CSF as previously described. Negative controls
425 were unstimulated bone marrow cells cultured in RPMI with 10% FBS. BMCs were incubated
426 with the various condition media for up to 72 h after which they were collected, and viability was
427 analyzed using trypan blue exclusion. BMCs were then washed, Fc-blocked, and stained with
428 panel of fluorescent markers to identify specific immune cell populations (please see tables).
429 Following staining, cells were resuspended in 200 μL FACS buffer and analyzed on a five-laser
430 BD FACS Fortessa (BD Biosciences, San Jose, CA, USA). FCS files were exported, and
431 compensation and analysis were conducted using FlowJo v9.7.

432

433 Immunofluorescent staining

434 Formalin-fixed paraffin-embedded samples were cut at 5 μm thickness. Sections were
435 deparaffinized through successive washes in: xylene (5 min), 100% ethanol (1 min), 90% ethanol
436 (1min), 70% ethanol with 0.25% NH_3 (1 hr), 50% ethanol (1min), water (1min). Slides were then
437 incubated in heated antigen retrieval buffer (10 mM sodium citrate, 0.05% Tween 20, pH 6.0) for
438 30min and then rinsed in running water. Slides were then removed, tissues circled with Immedge
439 pen and then incubated in blocking buffer (3% goat serum, 1% BSA, 1% cold fish skin gelatin,
440 0.1% Triton X-100, 0.05% tween 20, in 1x PBS, pH 7.2) for 30 min at room temperature.
441 Following three washes in PBS, slides were incubated in Sudan Black for 30 sec followed by
442 three PBS washes. Sections were incubated in primary antibody and maintained in a humidified
443 chamber overnight at +4°C. The following day, slides were washed three times with PBS and

444 incubated in secondary antibody, maintained in a humidified and dark chamber at room
445 temperature for 1h. Slides were washed three times with PBS, incubated and coverslips were
446 mounted using ProLong Glass antifade mounting medium (ThermoFisher, # P36980). Samples
447 were analyzed by confocal microscopy (Nikon A1 TIRF).

448

449 Antibodies used for immunofluorescent staining

450 Rabbit anti-mouse SP antibody (Thermo Fisher Scientific Cat# PA5-106934,
451 RRID:AB_2854598) used at 1:1000; Rabbit anti-ATF3 antibody (Thermo Fisher Scientific Cat#
452 PA5-106898, RRID:AB_2854562) used at 1: 500.

453

454 Substance P ELISA

455 Condition media were collected from mEERL cells, DRG, or their co-culture. Co-cultures were
456 generated as follows. Each co-culture contained 3 – 4 DRG which were extracted from C57BL/6
457 mice as previously described. DRG were placed onto Matrigel which was dropped on a 35 mm
458 dish. DRG/Matrigel dishes were left undisturbed overnight in an incubator. The following day,
459 1×10^6 mEERL cells were plate along the periphery of the Matrigel/DRG and the co-culture
460 incubated for 48 hrs before collection. Condition media for single cultures was collected from
461 mEERL cells when plates were 80% confluent and from DRG following 48 – 72h after being
462 plated on Matrigel. The concentration of SP in harvested condition media was estimated using a
463 standard curve with a SP EIA kit from RayBiotech (catalog# EIA-SP).

464

465 IL-6 ELISA

466 Condition media from mEERL cells alone, DRG alone, or their co-culture were harvested as
467 described for the SP ELISA. For determination of SP mediated IL-6 release, mEERL cells were
468 plated on 35 mm dishes in serum-free media overnight. The following day, 50 nM substance P
469 (Sigma Aldrich, acetate salt hydrate, Cat#S6883) alone, or with 100 uM NK1R antagonist (Tocris
470 Bioscience, L-732,138) was added. Cells were incubated with treatment for 48h prior to
471 conducting IL-6 ELISA which was performed as per manufacturer directions (RD Systems, cat #
472 M6000B).

473

474 Cytokine array

475 Cytokine arrays were purchased from RayBiotech (catalog # AAM-CYT-3). Condition media
476 were harvested from *in vitro* cultures of DRG alone, mEERL cells alone, or culture of mEERL
477 cells with DRG as described above. Cytokine arrays were processed per manufacturer's
478 recommendations. Briefly, arrays were blocked at room temperature and then treated with
479 undiluted condition media overnight at 4°C. The following day, arrays were treated with
480 biotinylated antibody cocktail for 2 h at room temperature, and then incubated for 2 h with HRP-
481 Streptavidin diluted in blocking buffer. Arrays were treated with detection buffer and imaged on a
482 Li-COR Odyssey imaging system.

483

484 Antibodies used for flow cytometry

485 The antibodies used for flow cytometry are listed in the table. A live/dead stain (Invitrogen,
486 Fixable blue cat. # L34962) was also used.

487 *Table A:*

488

Antibody	Vendor	Catalogue #	RRID
Anti-CD8	BioLegend	100712	AB_312751
Anti-PD-1-PE-Cy7	BioLegend	109110	AB_572017
Anti-LAG3-PE	BioLegend	125208	AB_2133343
Anti-TIM3-PerCP/Cyanine5.5	BioLegend	134012	AB_2632736
IFN γ -FITC	BioLegend	505806	AB_315400
TNF-BV510	BioLegend	506339	AB_2563127
IL-2-Pacific Blue	BioLegend	503820	AB_2127161
CD45.2-AF488	BioLegend	109815	AB_492869
CD3-BV510	BioLegend	100233	AB_2561387
CD4-BV421	BioLegend	100543	AB_10898318
MHCII-APC	eBioscience	17-5321-82	AB_469455
NKp46-PECy7	BioLegend	137617	AB_11218594
CD11b-PE	eBioscience	12-0112-81	AB_465546
CD8a-APCCy7	BioLegend	100713	AB_312752
CD11c-BV785	BioLegend	117335	AB_11219204
CD25-PerCPcy5.5	eBioscience	45-0251-80	AB_914323
GR-1-AF700	BioLegend	108421	AB_493728
F4v/80-BV605	BioLegend	123133	AB_2562305
CD45.2-BV605	BioLegend	109841	AB_2563485
MHCII-PE-Cy7	BioLegend	107629	AB_2290801
CD11b-PE-Cy5	BioLegend	101210	AB_312793
Ly6G-AF700	BioLegend	127622	AB_10643269
Ly6C-FITC	BioLegend	128005	AB_1186134
CD3-PE	BioLegend	100206	AB_312663
CD4-APC	eBioscience	17-0042-82	AB_469323
CD8a-BV421	BioLegend	100753	AB_2562558
CD335 NKp46-BV510	BioLegend	137623	AB_2563290

489

490 *Tumor dissociation and flow cytometry*

491 *In vivo* studies utilized 8-week-old male C57BL/6 or TRPV1^{cre::DTA}^{fl/wt} mice. For the
 492 experimental procedure, 100,000 mEERL cells were orthotopically injected into the oral cavity,
 493 following previously established methods and as described above (10, 80). Twenty-five days after
 494 the injection, the mice were euthanized, and the tumors were harvested. The tumors were then
 495 processed according to the MACS Tumor Dissociation protocol to ensure a single-cell suspension
 496 suitable for subsequent analyses. Cell viability post-dissociation was assessed using TO-PRO-3
 497 staining (Thermo Fisher, cat# T3605), and viable cells were sorted using an Accuri flow
 498 cytometer. For phenotypic analysis of the tumor-infiltrating cells, 1x10⁶ cells were stained with
 499 one of three fluorescent antibody panels. The panels used included a 12-color panel, a 9-color
 500 panel specifically designed for Ly6C/G identification, and a 4-color panel, detailed in
 501 accompanying tables. Flow cytometry data files were then compensated and analyzed using
 502 FlowJo software, providing detailed insights into the cellular composition and immune phenotype

503 of the tumor microenvironment. This comprehensive approach allows for a robust assessment of
504 the impact of tumor and immune cell interactions within the tumor microenvironment.

505 Co-culture of sEVs and DRG neurons

506 DRG were extracted from male C57BL/6 mice and placed into complete DMEM medium
507 (Corning, 10-013-CV) supplemented with 50 U/ml penicillin, 50 µg/ml streptomycin (Corning,
508 MT-3001-CI), and 10% FBS (Seradigm, 3100). The neurons were then dissociated using
509 phosphate-buffered saline (Corning, 21-040-CV) enriched with 1 mg/ml collagenase IV (Sigma,
510 C0130) and 2.4 U/ml dispase II (Sigma, 04942078001). This mixture was incubated for 80 min at
511 37°C. Afterward, the ganglia were triturated using glass Pasteur pipettes of decreasing sizes in
512 complete DMEM, followed by centrifugation over a 10% BSA gradient. The cells were then
513 plated on cell culture dishes coated with laminin (Sigma, L2020).

514
515
516 The plated cells were cultured in DMEM medium (Gibco, 21103-049) completed with 10% FBS,
517 1% penicillin–streptomycin, non-essential amino acids (Corning, 25-025-CI), and additional
518 supplements including β-mercaptoethanol (Gibco, 21985-023), L-glutamine (VWR, 02-0131),
519 0.05 ng/µl sodium pyruvate (Corning, 25-000-CI), a specified concentration of NGF (Life
520 Technologies, 13257-019), and 0.002 ng/µl GDNF (PeproTech, 450-51-10). After 2h, the cells
521 were co-cultured either with small extracellular vesicles (sEVs; 3 µg in 200 µl) or PBS, both in
522 the presence of a peptidase inhibitor (1 µM). Conditioned media were collected after 48h for
523 further analysis.

524 Isolation of sEVs

525 sEVs from mEERL cells were isolated by differential ultracentrifugation as previously described
526 (26). Briefly, conditioned media from mEERL cells was collected and spun in a Thermo Legend
527 X1R centrifuge at 300 x g for 10 min. The supernatant was collected and spun at 2000 x g for 10
528 min. The supernatant was collected and spun in a Sorval RC6 centrifuge at 10,000 x g for 30 min.
529 The supernatant was collected and spun in a Sorval WX80 Ultracentrifuge at 110,000 x
530 g for 2 h. The resulting pellet contains the sEVs and was washed with sterile PBS and spun again
531 (110,000 x g, 2 hrs). The supernatant was discarded and the pellet (sEVs) resuspended in 200 µl of
532 sterile PBS, aliquoted and stored at -80 °C until used. sEVs were validated by Nanosight particle
533 analysis.

534 Co-culture of CD8⁺ T cells and DRG neurons condition media.

535
536 Spleens were harvested from naïve male mice into cold PBS supplemented with 5% FBS and kept
537 on ice. The tissues were mechanically dissociated and then passed through a 70 µm strainer. Red
538 blood cells were lysed using RBC lysis buffer (Life Technologies, A1049201) for 2 min, and the
539 remaining cells were counted using a hemocytometer. Splenocytes were isolated via magnetic
540 sorting using a specific kit (Stem Cell, 19853A) and subsequently cultured in DMEM
541 supplemented with 10% FBS, 1% penicillin–streptomycin, non-essential amino acids (Corning,
542 25-025-CI), β-mercaptoethanol (Gibco, 21985-023), L-glutamine (VWR, 02-0131), and sodium
543 pyruvate (Corning, 25-000-CI).

544
545
546 The splenocytes were then stimulated under Tc1 conditions using 2 µg/ml of anti-CD3 and anti-
547 CD28 antibodies (Bio X Cell, BE00011, BE00151), 10 ng/ml recombinant IL-12 (BioLegend,
548 577008), and 10 µg/ml anti-IL-4 antibody (Bio X Cell, BE0045), in a 96-well plate. After 48 h of
549 stimulation, the cells were transferred to uncoated plates and exposed to either purified sEVs or
550 conditioned media from sEV/DRG neuron co-cultures for an additional 72 h.

552 Subsequently, the expression of checkpoint proteins PD-1, LAG3, and TIM3, as well as the
553 secretion of cytokines IFN γ , TNF α , and IL-2, were analyzed using flow cytometry, specifically
554 using an LSRFortessa or a FACSCanto II (Becton Dickinson). The quantification of cytokine
555 expression was performed after *in vitro* stimulation, providing detailed insights into the functional
556 status of the CD8⁺ T cells in response to the experimental treatments. This comprehensive
557 approach facilitates a deeper understanding of how CD8⁺ T cell functionality can be modulated by
558 external factors such as sEVs and DRG neuron-derived signals within the immune
559 microenvironment.

560 Intracellular cytokine staining.

561 Cytotoxic CD8⁺ T cells were stimulated with phorbol-12-myristate 13-acetate (PMA; 50 ng/ml,
562 Sigma-Aldrich, P1585), ionomycin (1 μ g/ml, Sigma-Aldrich, I3909), and Golgi Stop (1:100, BD
563 Biosciences, 554724) for 3 h to activate them and halt protein transport, enabling cytokine
564 accumulation. After stimulation, the cells were washed with FACS buffer, which consists of PBS
565 supplemented with 2% fetal calf serum and EDTA. This was followed by staining the cells with
566 Viability Dye eFluor 780 (eBioscience, 65-0865-14) for 15 min at 4°C to assess cell viability.

567
568 Post viability staining, the cells underwent another round of washing and were then stained for 30
569 min at 4°C with several antibodies: anti-CD8-APC (BioLegend, 100712), anti-PD-1-PE-Cy7
570 (BioLegend, 109110), anti-LAG3-PE (BioLegend, 125208), and anti-TIM3-PerCP/Cyanine5.5
571 (BioLegend, 134012). These stains were used to identify the CD8⁺ T cells and to evaluate their
572 expression of various immune checkpoint proteins.
573

574
575 Following surface staining, the cells were fixed and permeabilized using a kit (BD Biosciences,
576 554714) to allow for intracellular staining. The cells were then stained for IFN γ -FITC
577 (BioLegend, 505806), TNF-BV510 (BioLegend, 506339), and IL-2-Pacific Blue (BioLegend,
578 503820) to detect the production of key cytokines that indicate cellular activation and function.
579 The final analysis of the stained cells was conducted using flow cytometry, employing either a
580 LSRFortessa or FACSCanto II system (Becton Dickinson), providing detailed insights into the
581 functional status and health of the CD8⁺ T cells in response to stimulation. This multi-parameter
582 flow cytometry approach is essential for understanding the immune functionality and regulation
583 of cytotoxic T cells under various conditions.
584

585 RNA sequencing of triple co-cultures and data processing.

586 Naive TRPV1^{cre}::tdTomato^{fl/wt} DRG neurons, specifically 4×10^4 in number, were co-cultured
587 (1:10 ratio) with mEERL-derived small extracellular vesicles (sEVs), CD8⁺ T cells, or a
588 combination of both, each within T cell medium. The medium was supplemented with
589 neurotrophic factors: 0.05 ng/ μ l neuron growth factor (NGF) from Life Technologies (Cat#
590 13257019) and 0.002 ng/ μ l glial cell line-derived neurotrophic factor (GDNF) from PeproTech
591 (Cat# 450-51-10), to support neuronal survival and function.
592

593 After 48 h of co-culturing, the cells were collected, and the TRPV1-expressing neurons,
594 identifiable by their tdTomato fluorescence, were purified using a FACSARIA IIu cell sorter
595 (Becton Dickinson). This sorting process ensures that subsequent analyses or experiments are
596 conducted on a homogeneous population of TRPV1⁺ neurons, eliminating any non-neuronal or
597 non-TRPV1-expressing cells that could confound results. This methodical approach facilitates the
598 study of specific interactions between DRG neurons and immune cells or factors within the
599 controlled conditions of an *in vitro* system.
500

501 RNA-sequencing libraries of TRPV1 neurons were constructed using the Illumina TruSeq
502 Stranded RNA LT Kit, adhering closely to the manufacturer's instructions provided by Illumina.
503 Sequencing of these libraries was carried out at Fulgent Genetics. The sequencing reads were then
504 aligned to the Mouse mm10 reference genome (GenBank assembly accession
505 GCA_000001635.2) using the STAR software version 2.7. After alignment, reads that mapped to
506 genic regions were quantified using the featureCounts function from the subread package version
507 1.6.4.

508
509 Gene expression levels across the samples were quantified in terms of Transcripts Per Million
510 (TPM), which facilitates comparison between samples by normalizing for both sequencing depth
511 and gene length. Hierarchical clustering of gene expression data was performed using the
512 heatmap.2 function from the gplots package in R (version 3.1.3), employing the ward.D2 method
513 to discern patterns and relationships in gene expression among the samples. For differential gene
514 expression analysis, DeSeq2 version 1.28.1 was utilized to identify genes that were significantly
515 upregulated or downregulated under different experimental conditions. The results of these
516 analyses, including all relevant data, have been deposited in the NCBI's Gene Expression
517 Omnibus (GEO), accessible under the accession number GSE205864. This comprehensive
518 approach provides a robust framework for understanding the transcriptional changes in TRPV1
519 neurons in response to various experimental treatments.

520 521 Quantitative polymerase chain reaction for MDSC genes

522 Real-time quantitative reverse transcription (RT-qPCR) was conducted to analyze the levels of
523 MDSC-associated transcripts in the generated MDSC populations. The process began with the
524 extraction of total RNA using Qiazol extraction reagent, followed by further purification through
525 phenol-chloroform extraction protocols. The quality and quantity of the extracted RNA were
526 assessed using a NanoDrop spectrophotometer. Subsequently, cDNAs were synthesized from the
527 RNA samples using a High-Capacity cDNA Reverse Transcription kit from Applied Biosciences.
528 Gene expression analysis was performed using real-time quantitative RT-PCR on a CFX-96
529 system from BioRad. Specific primers used for amplifying the gene products are detailed above.
530 The mRNA levels of the genes of interest were quantified using the comparative threshold cycle
531 (Ct) method. This involves normalizing the expression level of each gene of interest to that of a
532 housekeeping gene, β -actin, to account for variations in RNA input and efficiency of the RT
533 reaction across different samples. This normalization is crucial for accurate, reproducible, and
534 meaningful quantification of gene expression, facilitating the comparison of mRNA levels across
535 different experimental conditions and samples.

536 537 Statistical analysis

538 GraphPad Prism (version 10.0.3,
539 2023) was used for all statistical
540 analyses. The specific statistical
541 tests for each experiment are
542 noted below in the corresponding
543 figure legend.

Primer	Sequence (5' – 3')
ARG1 FWD	ACAGCAAAGCAGACAGAACTA
ARG1 REV	GAAAGGAACTGCTGGGATACA
COX2 FWD	CGGACTGGATTCTATGGTGAAA

544

545 Tumor growth curves: Two-way
546 ANOVA with post-hoc Tukey
547 test or two-sided unpaired
548 Student's t-test.

COX2 REV	CTTGAAGTGGGTCAGGATGTAG
CYBB FWD	CTTTGGTACAGCCAGTGAAGA
CYBB REV	CCAGACAGACTTGAGAATGAG

549 Gene/protein expression differences: Student's t-test or one-way ANOVA with post-hoc Tukey
550 test.

551 ELISA: One-way ANOVA with post-hoc Tukey test.

552 Flow cytometry data: Two-sided unpaired Student's t-test or one-way ANOVA with post-hoc
553 Tukey test.

554 MDSC migration assay: One-way ANOVA with post-hoc Tukey test.

555

556

557 **References**

558

- 559 1. M. S. Longworth, L. A. Laimins, Pathogenesis of human papillomaviruses in
560 differentiating epithelia. *Microbiol Mol Biol Rev* **68**, 362-372 (2004).
- 561 2. W. R. McIlwain, A. J. Sood, S. A. Nguyen, T. A. Day, Initial symptoms in patients with
562 HPV-positive and HPV-negative oropharyngeal cancer. *JAMA Otolaryngol Head Neck*
563 *Surg* **140**, 441-447 (2014).
- 564 3. D. E. Johnson *et al.*, Head and neck squamous cell carcinoma. *Nat Rev Dis Primers* **6**, 92
565 (2020).
- 566 4. R. L. Siegel, K. D. Miller, A. Jemal, Cancer Statistics, 2017. *CA Cancer J Clin* **67**, 7-30
567 (2017).
- 568 5. A. R. Cillo *et al.*, Immune Landscape of Viral- and Carcinogen-Driven Head and Neck
569 Cancer. *Immunity* **52**, 183-199 e189 (2020).
- 570 6. H. A. Qureshi *et al.*, Impact of HPV status on immune responses in head and neck
571 squamous cell carcinoma. *Oral Oncol* **127**, 105774 (2022).
- 572 7. V. Sridharan *et al.*, Definitive chemoradiation alters the immunologic landscape and
573 immune checkpoints in head and neck cancer. *Br J Cancer* **115**, 252-260 (2016).
- 574 8. Y. Sun, Z. Wang, S. Qiu, R. Wang, Therapeutic strategies of different HPV status in Head
575 and Neck Squamous Cell Carcinoma. *Int J Biol Sci* **17**, 1104-1118 (2021).
- 576 9. C. W. Wang, P. K. Biswas, A. Islam, M. K. Chen, P. J. Chueh, The Use of Immune
577 Regulation in Treating Head and Neck Squamous Cell Carcinoma (HNSCC). *Cells* **13**,
578 (2024).
- 579 10. A. C. Restaino *et al.*, Functional neuronal circuits promote disease progression in cancer.
580 *Sci Adv* **9**, eade4443 (2023).
- 581 11. P. Marz *et al.*, Sympathetic neurons can produce and respond to interleukin 6. *Proc Natl*
582 *Acad Sci U S A* **95**, 3251-3256 (1998).
- 583 12. A. Azzolina, A. Bongiovanni, N. Lampiasi, Substance P induces TNF-alpha and IL-6
584 production through NF kappa B in peritoneal mast cells. *Biochim Biophys Acta* **1643**, 75-
585 83 (2003).
- 586 13. I. M. Chiu *et al.*, Bacteria activate sensory neurons that modulate pain and inflammation.
587 *Nature* **501**, 52-57 (2013).
- 588 14. F. A. Pinho-Ribeiro *et al.*, Blocking Neuronal Signaling to Immune Cells Treats
589 Streptococcal Invasive Infection. *Cell* **173**, 1083-1097 e1022 (2018).
- 590 15. R. Terenzi *et al.*, Neuropeptides activate TRPV1 in rheumatoid arthritis fibroblast-like
591 synoviocytes and foster IL-6 and IL-8 production. *Ann Rheum Dis* **72**, 1107-1109 (2013).
- 592 16. M. Ebbinghaus *et al.*, Interleukin-6-dependent influence of nociceptive sensory neurons
593 on antigen-induced arthritis. *Arthritis Res Ther* **17**, 334 (2015).

- 594 17. Y. Hou *et al.*, The neurotransmitter calcitonin gene-related peptide shapes an
595 immunosuppressive microenvironment in medullary thyroid cancer. *Nat Commun* **15**,
596 5555 (2024).
- 597 18. M. Balood *et al.*, Nociceptor neurons affect cancer immunosurveillance. *Nature*, (2022).
- 598 19. L. A. McIlvried, M. A. Atherton, N. L. Horan, T. N. Goch, N. N. Scheff, Sensory
599 Neurotransmitter Calcitonin Gene-Related Peptide Modulates Tumor Growth and
700 Lymphocyte Infiltration in Oral Squamous Cell Carcinoma. *Adv Biol (Weinh)*, e2200019
701 (2022).
- 702 20. R. Kalluri, V. S. LeBleu, The biology, function, and biomedical applications of exosomes.
703 *Science* **367**, (2020).
- 704 21. R. Kalluri, The biology and function of exosomes in cancer. *J Clin Invest* **126**, 1208-1215
705 (2016).
- 706 22. L. Mashouri *et al.*, Exosomes: composition, biogenesis, and mechanisms in cancer
707 metastasis and drug resistance. *Molecular cancer* **18**, 75 (2019).
- 708 23. Q. Song *et al.*, Bladder cancer-derived exosomal KRT6B promotes invasion and
709 metastasis by inducing EMT and regulating the immune microenvironment. *J Transl Med*
710 **20**, 308 (2022).
- 711 24. Z. Jing, K. Chen, L. Gong, The Significance of Exosomes in Pathogenesis, Diagnosis, and
712 Treatment of Esophageal Cancer. *Int J Nanomedicine* **16**, 6115-6127 (2021).
- 713 25. A. Hoshino *et al.*, Tumour exosome integrins determine organotropic metastasis. *Nature*
714 **527**, 329-335 (2015).
- 715 26. M. Madeo *et al.*, Cancer exosomes induce tumor innervation. *Nat Commun* **9**, 4284
716 (2018).
- 717 27. M. Amit *et al.*, Loss of p53 drives neuron reprogramming in head and neck cancer. *Nature*
718 **578**, 449-454 (2020).
- 719 28. N. L. Horan *et al.*, The impact of tumor immunogenicity on cancer pain phenotype using
720 syngeneic oral cancer mouse models. *Front Pain Res (Lausanne)* **3**, 991725 (2022).
- 721 29. R. Weber *et al.*, IL-6 as a major regulator of MDSC activity and possible target for cancer
722 immunotherapy. *Cell Immunol* **359**, 104254 (2021).
- 723 30. T. Kato *et al.*, Cancer-Associated Fibroblasts Affect Intratumoral CD8(+) and FoxP3(+) T
724 Cells Via IL6 in the Tumor Microenvironment. *Clin Cancer Res* **24**, 4820-4833 (2018).
- 725 31. B. Jing *et al.*, IL6/STAT3 Signaling Orchestrates Premetastatic Niche Formation and
726 Immunosuppressive Traits in Lung. *Cancer Res* **80**, 784-797 (2020).
- 727 32. C. Vanhaver, P. van der Bruggen, A. M. Bruger, MDSC in Mice and Men: Mechanisms of
728 Immunosuppression in Cancer. *J Clin Med* **10**, (2021).
- 729 33. L. Cassetta *et al.*, Deciphering myeloid-derived suppressor cells: isolation and markers in
730 humans, mice and non-human primates. *Cancer Immunol Immunother* **68**, 687-697
731 (2019).
- 732 34. K. Alicea-Torres *et al.*, Immune suppressive activity of myeloid-derived suppressor cells
733 in cancer requires inactivation of the type I interferon pathway. *Nat Commun* **12**, 1717
734 (2021).
- 735 35. Y. Zhao, T. Wu, S. Shao, B. Shi, Y. Zhao, Phenotype, development, and biological
736 function of myeloid-derived suppressor cells. *Oncoimmunology* **5**, e1004983 (2016).
- 737 36. E. Tcyganov, J. Mastio, E. Chen, D. I. Gabrilovich, Plasticity of myeloid-derived
738 suppressor cells in cancer. *Current opinion in immunology* **51**, 76-82 (2018).
- 739 37. L. Yang, C. M. Edwards, G. R. Mundy, Gr-1+CD11b+ myeloid-derived suppressor cells:
740 formidable partners in tumor metastasis. *J Bone Miner Res* **25**, 1701-1706 (2010).
- 741 38. T. M. Grzywa *et al.*, Myeloid Cell-Derived Arginase in Cancer Immune Response. *Front*
742 *Immunol* **11**, 938 (2020).

- 743 39. H. Zhou *et al.*, Modified method for differentiation of myeloid-derived suppressor cells in
744 vitro enhances immunosuppressive ability via glutathione metabolism. *Biochem Biophys*
745 *Rep* **33**, 101416 (2023).
- 746 40. E. P. Chen *et al.*, Myeloid Cell COX-2 deletion reduces mammary tumor growth through
747 enhanced cytotoxic T-lymphocyte function. *Carcinogenesis* **35**, 1788-1797 (2014).
- 748 41. J. Liu *et al.*, Immune suppressed tumor microenvironment by exosomes derived from
749 gastric cancer cells via modulating immune functions. *Sci Rep* **10**, 14749 (2020).
- 750 42. C. Viallard, B. Larrivee, Tumor angiogenesis and vascular normalization: alternative
751 therapeutic targets. *Angiogenesis* **20**, 409-426 (2017).
- 752 43. R. Lugano, M. Ramachandran, A. Dimberg, Tumor angiogenesis: causes, consequences,
753 challenges and opportunities. *Cell Mol Life Sci* **77**, 1745-1770 (2020).
- 754 44. M. Abbott, Y. Ustoyev, Cancer and the Immune System: The History and Background of
755 Immunotherapy. *Semin Oncol Nurs* **35**, 150923 (2019).
- 756 45. S. Greene, P. Patel, C. T. Allen, How patients with an intact immune system develop head
757 and neck cancer. *Oral Oncol* **92**, 26-32 (2019).
- 758 46. Y. C. Lu, X. J. Wang, Harnessing the power of the immune system in cancer
759 immunotherapy and cancer prevention. *Mol Carcinog* **59**, 675-678 (2020).
- 760 47. P. Hanc *et al.*, Multimodal control of dendritic cell functions by nociceptors. *Science* **379**,
761 eabm5658 (2023).
- 762 48. S. B. Théo Crosson, Jo-Chiao Wang, Clara Salaun, Katiane Roversi, Herbert Herzog,
763 Moutih Rafei, Rikard Blunck, Sebastien Talbot. (2023).
- 764 49. N. Kitamura *et al.*, Current Trends and Future Prospects of Molecular Targeted Therapy in
765 Head and Neck Squamous Cell Carcinoma. *Int J Mol Sci* **22**, (2020).
- 766 50. A. W. Y. Chai, K. P. Lim, S. C. Cheong, Translational genomics and recent advances in
767 oral squamous cell carcinoma. *Seminars in cancer biology* **61**, 71-83 (2020).
- 768 51. H. Ge, R. L. Ferris, J. H. Wang, Cetuximab Responses in Patients with HNSCC Correlate
769 to Clonal Expansion Feature of Peripheral and Tumor-Infiltrating T Cells with Top T-Cell
770 Receptor Clonotypes. *Clin Cancer Res* **29**, 647-658 (2023).
- 771 52. H. Mehanna *et al.*, Radiotherapy plus cisplatin or cetuximab in low-risk human
772 papillomavirus-positive oropharyngeal cancer (De-ESCALaTE HPV): an open-label
773 randomised controlled phase 3 trial. *Lancet* **393**, 51-60 (2019).
- 774 53. L. Sun *et al.*, Cetuximab-Based vs Carboplatin-Based Chemoradiotherapy for Patients
775 With Head and Neck Cancer. *JAMA Otolaryngol Head Neck Surg* **148**, 1022-1028 (2022).
- 776 54. A. Bhatia, B. Burtness, Treating Head and Neck Cancer in the Age of Immunotherapy: A
777 2023 Update. *Drugs* **83**, 217-248 (2023).
- 778 55. Y. Chen *et al.*, The current advances and future directions of PD-1/PD-L1 blockade in
779 head and neck squamous cell carcinoma (HNSCC) in the era of immunotherapy. *Int*
780 *Immunopharmacol* **120**, 110329 (2023).
- 781 56. A. T. Ruffin *et al.*, Improving head and neck cancer therapies by immunomodulation of
782 the tumour microenvironment. *Nat Rev Cancer* **23**, 173-188 (2023).
- 783 57. J. Guigay *et al.*, Cetuximab, docetaxel, and cisplatin versus platinum, fluorouracil, and
784 cetuximab as first-line treatment in patients with recurrent or metastatic head and neck
785 squamous-cell carcinoma (GORTEC 2014-01 TPExtreme): a multicentre, open-label,
786 randomised, phase 2 trial. *Lancet Oncol* **22**, 463-475 (2021).
- 787 58. J. B. Weidhaas *et al.*, The KRAS-Variant and Cetuximab Response in Head and Neck
788 Squamous Cell Cancer: A Secondary Analysis of a Randomized Clinical Trial. *JAMA*
789 *Oncol* **3**, 483-491 (2017).
- 790 59. K. J. Harrington *et al.*, Pembrolizumab With or Without Chemotherapy in Recurrent or
791 Metastatic Head and Neck Squamous Cell Carcinoma: Updated Results of the Phase III
792 KEYNOTE-048 Study. *J Clin Oncol* **41**, 790-802 (2023).

- 793 60. B. Burtneß *et al.*, Pembrolizumab alone or with chemotherapy versus cetuximab with
794 chemotherapy for recurrent or metastatic squamous cell carcinoma of the head and neck
795 (KEYNOTE-048): a randomised, open-label, phase 3 study. *Lancet* **394**, 1915-1928
796 (2019).
- 797 61. I. Yaman, D. Agac Cobanoglu, T. Xie, Y. Ye, M. Amit, Advances in understanding
798 cancer-associated neurogenesis and its implications on the neuroimmune axis in cancer.
799 *Pharmacol Ther* **239**, 108199 (2022).
- 300 62. S. M. Gysler, R. Drapkin, Tumor innervation: peripheral nerves take control of the tumor
301 microenvironment. *J Clin Invest* **131**, (2021).
- 302 63. K. E. de Visser, J. A. Joyce, The evolving tumor microenvironment: From cancer
303 initiation to metastatic outgrowth. *Cancer cell* **41**, 374-403 (2023).
- 304 64. R. D. Cervantes-Villagrana, D. Albores-Garcia, A. R. Cervantes-Villagrana, S. J. Garcia-
305 Acevez, Tumor-induced neurogenesis and immune evasion as targets of innovative anti-
306 cancer therapies. *Signal Transduct Target Ther* **5**, 99 (2020).
- 307 65. N. N. Scheff, J. L. Saloman, Neuroimmunology of cancer and associated symptomology.
308 *Immunology and cell biology* **99**, 949-961 (2021).
- 309 66. A. C. Hoover *et al.*, The role of human papillomavirus 16 E6 in anchorage-independent
310 and invasive growth of mouse tonsil epithelium. *Arch Otolaryngol Head Neck Surg* **133**,
311 495-502 (2007).
- 312 67. W. C. Spanos *et al.*, The PDZ binding motif of human papillomavirus type 16 E6 induces
313 PTPN13 loss, which allows anchorage-independent growth and synergizes with ras for
314 invasive growth. *J Virol* **82**, 2493-2500 (2008).
- 315 68. P. Baral *et al.*, Nociceptor sensory neurons suppress neutrophil and gammadelta T cell
316 responses in bacterial lung infections and lethal pneumonia. *Nat Med* **24**, 417-426 (2018).
- 317 69. F. Michoud *et al.*, Epineural optogenetic activation of nociceptors initiates and amplifies
318 inflammation. *Nat Biotechnol* **39**, 179-185 (2021).
- 319 70. I. Monsellato *et al.*, Robotic transanal total mesorectal excision: A new perspective for
320 low rectal cancer treatment. A case series. *Int J Surg Case Rep* **61**, 86-90 (2019).
- 321 71. N. Y. Lai *et al.*, Gut-Innervating Nociceptor Neurons Regulate Peyer's Patch Microfold
322 Cells and SFB Levels to Mediate Salmonella Host Defense. *Cell* **180**, 33-49 e22 (2020).
- 323 72. H. J. Solinski *et al.*, Nppb Neurons Are Sensors of Mast Cell-Induced Itch. *Cell Rep* **26**,
324 3561-3573 e3564 (2019).
- 325 73. E. J. Cobos *et al.*, Mechanistic Differences in Neuropathic Pain Modalities Revealed by
326 Correlating Behavior with Global Expression Profiling. *Cell Rep* **22**, 1301-1312 (2018).
- 327 74. S. Talbot *et al.*, Vagal sensory neurons drive mucous cell metaplasia. *The Journal of*
328 *allergy and clinical immunology* **145**, 1693-1696 e1694 (2020).
- 329 75. D. Trankner, N. Hahne, K. Sugino, M. A. Hoon, C. Zuker, Population of sensory neurons
330 essential for asthmatic hyperreactivity of inflamed airways. *Proc Natl Acad Sci U S A* **111**,
331 11515-11520 (2014).
- 332 76. S. Mathur *et al.*, Nociceptor neurons promote IgE class switch in B cells. *JCI insight* **6**,
333 (2021).
- 334 77. S. L. Foster, C. R. Seehus, C. J. Woolf, S. Talbot, Sense and Immunity: Context-
335 Dependent Neuro-Immune Interplay. *Front Immunol* **8**, 1463 (2017).
- 336 78. C. Perner *et al.*, Substance P Release by Sensory Neurons Triggers Dendritic Cell
337 Migration and Initiates the Type-2 Immune Response to Allergens. *Immunity* **53**, 1063-
338 1077 e1067 (2020).
- 339 79. J. E. Choi *et al.*, Isolation of human and mouse myeloid-derived suppressor cells for
340 metabolic analysis. *STAR Protoc* **3**, 101389 (2022).
- 341 80. J. Barr *et al.*, Tumor-infiltrating nerves functionally alter brain circuits and modulate
342 behavior in a male mouse model of head-and-neck cancer. *bioRxiv*, (2024).

343

344 **Acknowledgments**

345 We thank the Flow Cytometry Core (Sanford Research, supported by National Institute of
346 General Medical Sciences, Center of Biomedical Research Excellence P30GM145398) for
347 their services and expertise towards this project.

348

349 **Funding:**

350 National Institute of Dental and Craniofacial Research grant R01DE032712 (PDV)

351 National Institute of General Medical Sciences grant P30GM103548 (PDV)

352 Canadian Institutes of Health Research grants 162211, 461274, 461275 (ST)

353

354 **Author contributions:**

355 Conceptualization: PDV, ST, ACR

356 Methodology: ACR, MA, AW,

357 Investigation: ACR, MA, AW

358 Visualization: TE, ARN, MB, ACR

359 Supervision: PDV, ST

360 Writing—original draft: PDV

361 Writing—review & editing: PDV, ST, ACR, MRN, MB, TE

362 Project administration: PDV, ST

363 Funding acquisition: PDV, ST

364 Formal analysis: TE, ARN

365

366 **Competing interests:** Sebastien Talbot is a minority stake holder in Nocion Therapeutics
367 and received funding from Nocion Therapeutics and Cygnal Therapeutics. All other
368 authors declare they have no competing interests.

369

370 **Data and materials availability:**

371 All data are available in the main text or the supplementary materials. Upon request, cell
372 lines will be made available following a materials transfer agreement (MTA). The RNA
373 sequencing dataset has been deposited in the NCBI's Gene Expression Omnibus (GEO),
374 accessible under the accession number GSE205864.

375

376

377

378

379

Figure 1

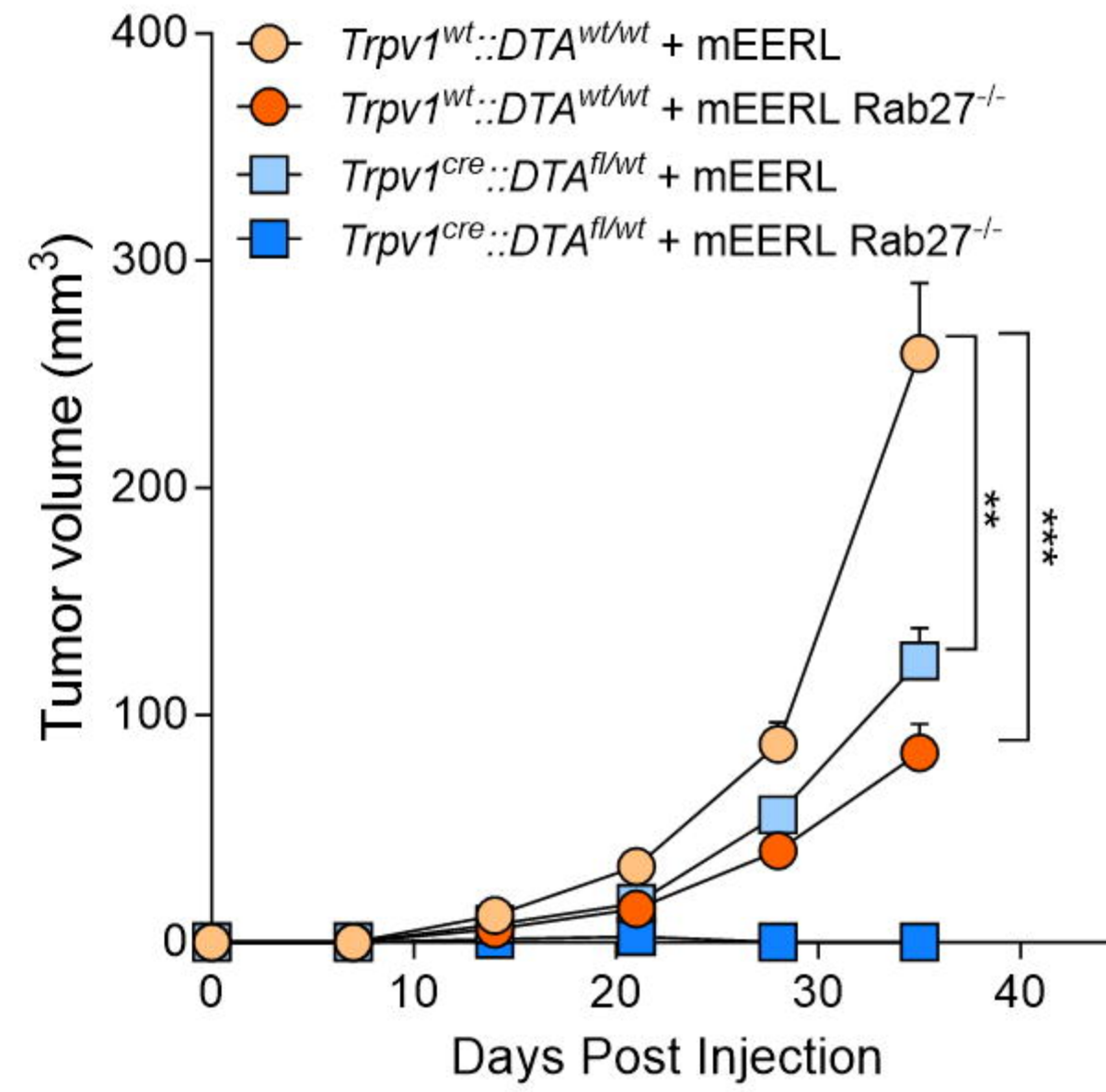


Figure 2

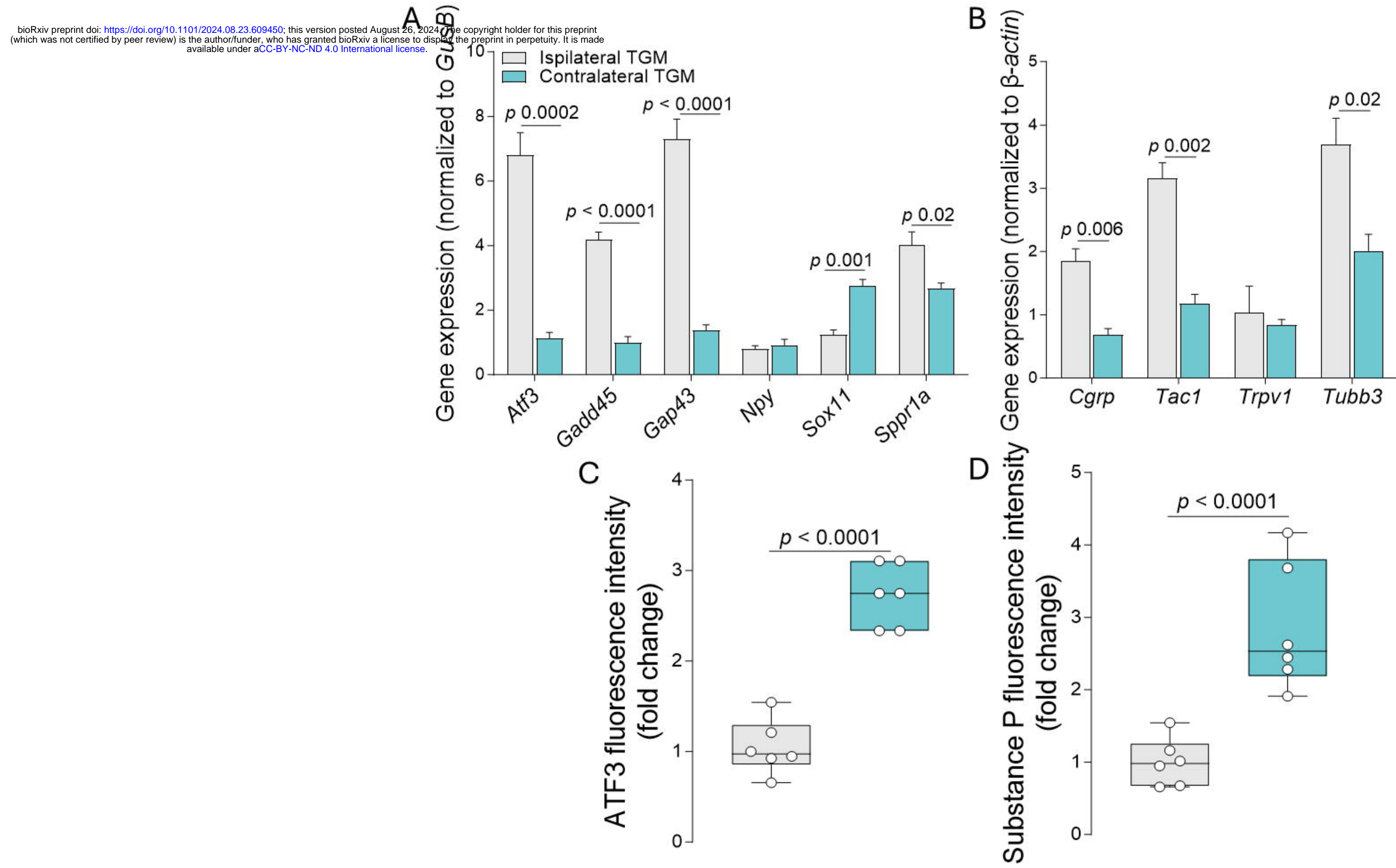


Figure 3

bioRxiv preprint doi: <https://doi.org/10.1101/2024.08.23.609450>; this version posted August 26, 2024. The copyright holder for this preprint (which was not certified by peer review) is the author/funder, who has granted bioRxiv a license to display the preprint in perpetuity. It is made available under aCC-BY-NC-ND 4.0 International license.

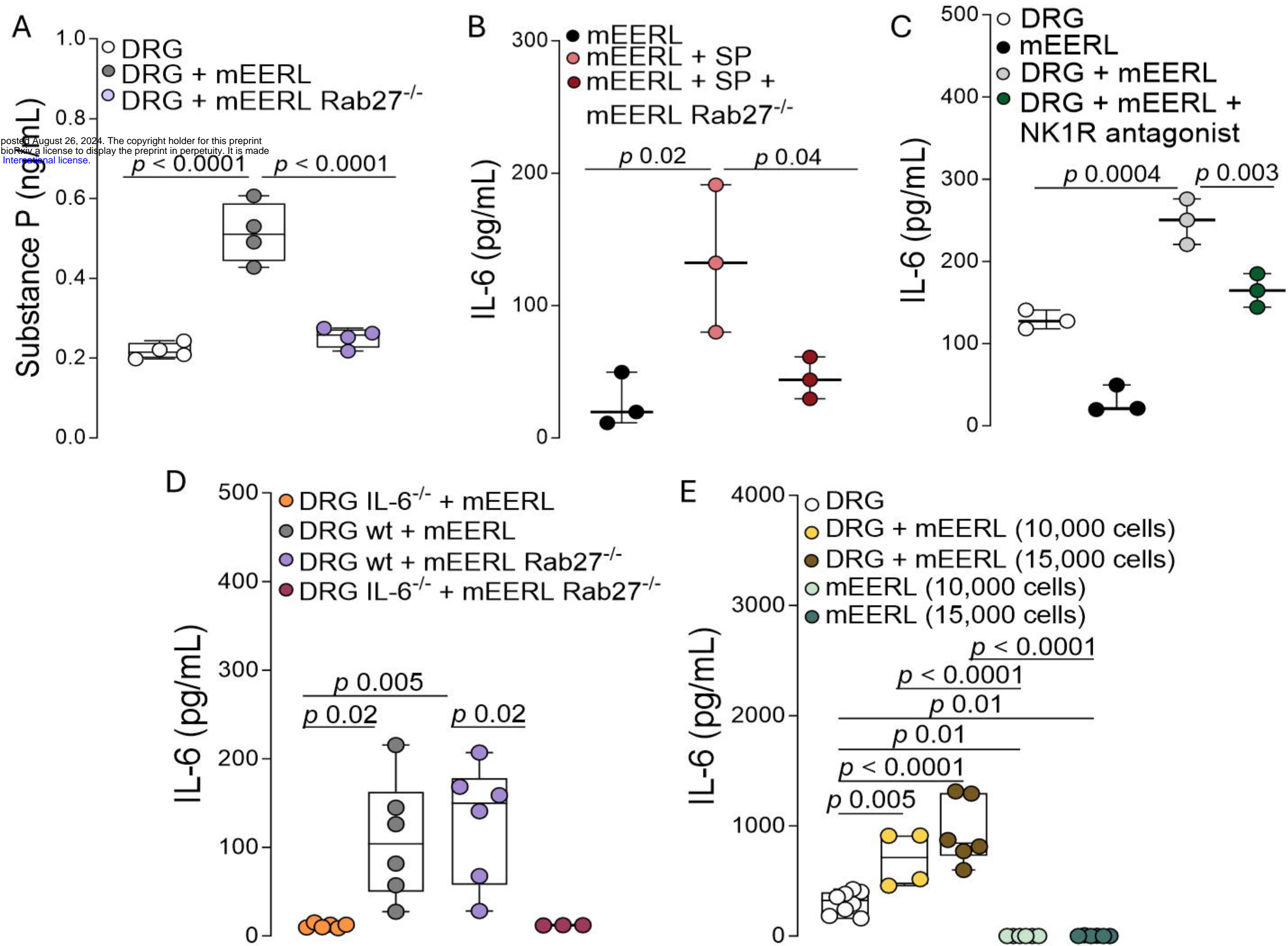


Figure 4

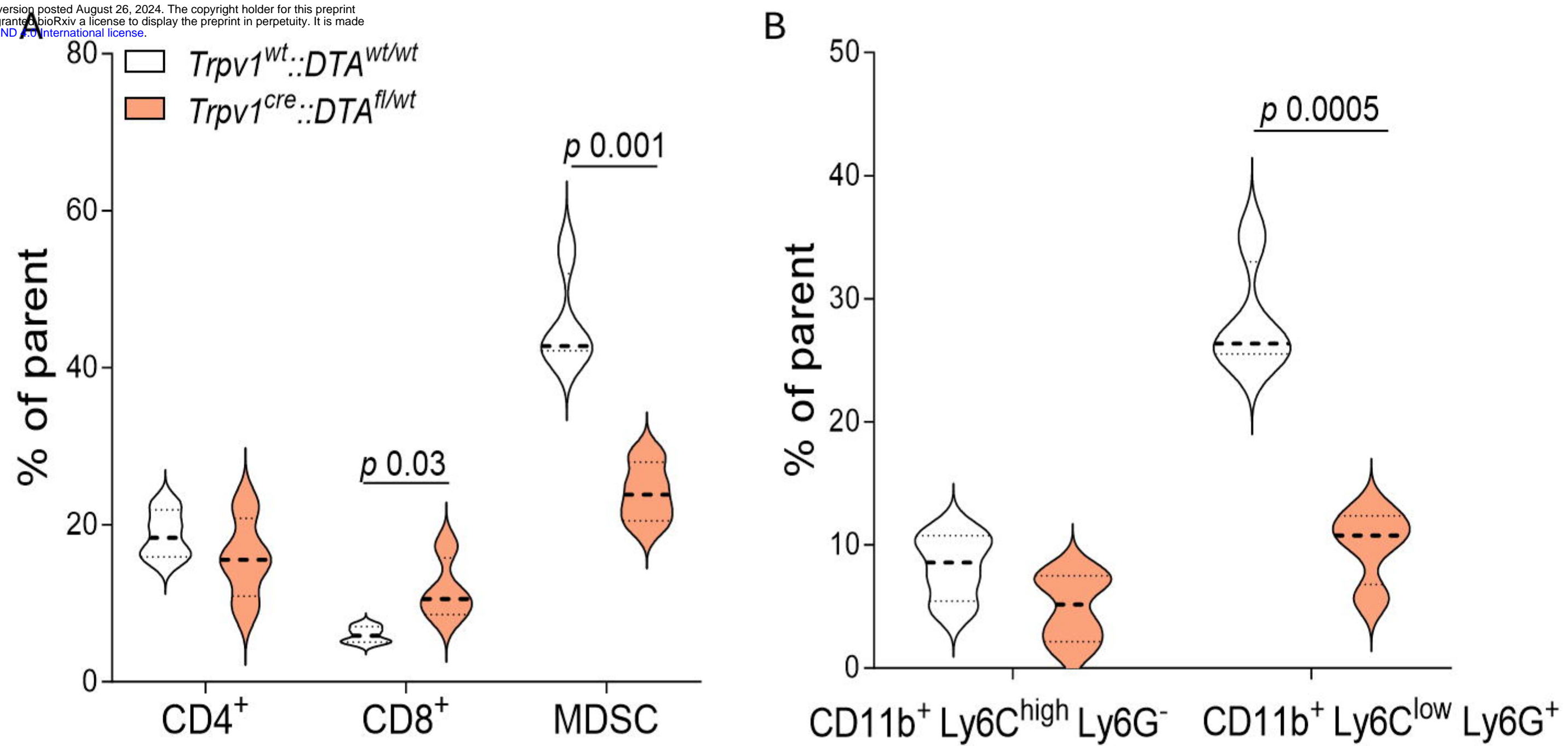


Figure 5

